Journal of Hydraulic Research Vol. 44, No. 4 (2006), pp. 437–450

Vortex trajectory hysteresis above self-formed vortex ripples

Hystérésis de trajectoires de tourbillons sur des rides auto-formées par des tourbillons

DAVID ADMIRAAL, Associate Professor, *Department of Civil Engineering, W355 Nebraska Hall, University of Nebraska, Lincoln, NE 68588-0531, USA. E-mail: dadmiraal@unl.edu*

RODRIGO MUSALEM-JARA, *South Florida Water Management District, 3301 Gun Club Road, West Palm Beach, FL 33401, USA. E-mail: rmusalem@sfwmd.gov*

MARCELO GARCÍA, Professor, *Department of Civil and Environmental Engineering, 205 North Mathews, University of Illinois, Urbana, IL 68501, USA. E-mail: mhgarcia@uiuc.edu*

YARKO NIÑO, Associate Professor, *Department of Civil Engineering, Universidad de Chile, Av. Blanco Encalada 2002, Santiago, Chile. E-mail: ynino@ing.uchile.cl*

ABSTRACT

Particle image velocimetry (PIV) using fluorescent tracer particles has been used to measure the velocity field of the fluid above self-formed vortex ripples in an oscillatory flow with suspended sediment. Measured velocities were used to find distributions of phase-averaged velocity and vorticity. Using the distributions, discrete vortices were then identified and tracked. Vortices that originated in the wakes of ripples were carried by the flow to adjacent ripples where they recombined with vortices being generated during the next half-cycle of the flow. Two possible states were observed for similar flow conditions, where vortex migration was either 0.9 or 1.5 ripple wavelengths before recombination. Evidence indicates that this may be the result of two possible ripple wavelengths: one that is approximately twice the flow amplitude, and one that is approximately 1.4 times the flow amplitude. The 2-D circulation strength of discrete vortices, defined as the integral of vorticity over the area of the vortex, was numerically estimated from PIV measurements. Maximum dimensionless values of circulation tend to increase as the Reynolds number of the oscillatory flow increases and to decrease as the mobility parameter (a dimensionless number that quantifies the sediment transport capacity of the oscillatory flow) increases. This is interpreted as an effect of enhanced dissipation of vorticity due to the presence of increasing concentrations of entrained sediment as the mobility number increases.

RÉSUMÉ

La vélocimétrie à images de particules (PIV) avec des particules traçantes fluorescentes a été utilisée pour mesurer le champ de vitesses sur des ondulations auto-fomées par des tourbillons dans un écoulement oscillant avec des sédiments en suspension. Les vitesses mesurées ont été utilisées pour déterminer les distributions de vitesses et tourbillons en moyenne de phase. En utilisant les distributions, les tourbillons discrets ont été ensuite identifiés et suivis. Des tourbillons engendrés dans le sillon des ondulations sont transportés par l'écoulement vers les ondulations adjacentes où ils se recombinent avec des tourbillons générés durant le demi cycle suivant de l'écoulement. Deux états possibles sont observés pour des conditions d'écoulement semblables, où les tourbillons migrent de 0.9 ou 1.5 fois la longueur d'onde avant recombinaison. Il est prouvé que cela peut être dû à deux longueurs d'onde des ondulations possibles: l'une est approximativement le double de l'amplitude de l'écoulement, l'autre 1.4 fois. L'intensité de la circulation 2-D des tourbillons discrets, définie comme l'intégrale de la vorticité sur le champ du tourbillon, a été estimée à partir des mesures PIV. Les valeurs maximales de circulation sans dimension, tendent à croître avec le nombre de Reynolds de l'écoulement oscillant et à décroître quand le paramètre de mobilité croît (un nombre sans dimension qui quantifie la capacité de transport de sédiment de l'écoulement oscillant). Ceci est interprété comme un effet accru de la dissipation du tourbillon dû à la présence croissante de concentrations de sédiments entraînés avec le paramètre de mobilité.

Keywords: Oscillatory flow, sediment transport, fluorescent tracers, PIV, sand ripples.

1 Introduction

Vortex sand ripples are bedforms created by oscillatory flows and are commonly generated beneath waves. The name "vortex ripple" refers to the vortices that originate on the lee side of the bedforms because of flow separation. As shown in Fig. 1, the ripples are uniformly spaced. The wavelength of the ripples is closely related to the amplitude of the oscillatory flow. Vortex ripples increase form drag, and flow separation and vortex shedding around the ripples greatly enhances the entrainment of sediment into suspension. This is particularly important considering that suspended sediment is a major component of near-shore

Revision received November 4, 2005/Open for discussion until August 31, 2007.

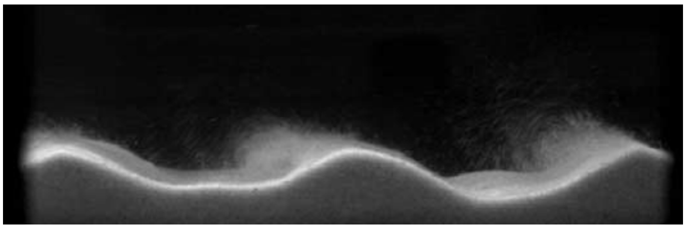

Figure 1 Vortex ripples in an experimental U-tube.

sediment transport (Sleath, 1984). Because of their importance, vortex ripples have been extensively studied (e.g., Fredsøe and Deigaard, 1992; Nielsen, 1992; Blondeaux, 2001; Ardhuin *et al.*, 2002; Nimmo Smith *et al.*, 2002). However, accurate prediction of important ripple properties has been precluded by the complexity of the flow field and sediment transport processes that surround them. For example, despite many investigations of the equilibrium wavelength of vortex ripples, it is still poorly understood (Andersen, 1999).

The study of vortex ripples includes the pioneering work of Ayrton (1910), who first recognized that vortices that form downstream of ripples play a significant role in vortex ripple development and behavior. Bagnold (1946) later distinguished between rolling grain ripples and vortex ripples, the latter of which experience flow separation downstream of the ripple crest. Since these investigations, many efforts have been made to describe the characteristics of the flow field above vortex ripples using analytical or numerical models. However, there are no complete descriptions, mainly due to the complex nonlinear interaction between the turbulent flow field around the bedforms and the associated sediment transport. Longuet-Higgins (1981) developed an irrotational model of vortex motion, assuming that ripple boundaries were stationary, and that suspended sand did not affect the flow. Despite these simplifications, Longuet-Higgens was able to satisfactorily predict form drag induced on the flow by the ripples, demonstrating that even an elementary understanding of vortex behavior can improve prediction of vortex ripple characteristics. The importance of ripple vortices has led others to utilize discrete vortex modeling in their numerical simulations as well (Hansen *et al.*, 1994; Perrier *et al.*, 1994). Blondeaux (1990) and Vittori and Blondeaux (1990) used linear and nonlinear stability analysis to predict the development of sand ripples beneath an oscillatory flow. Their analysis was limited to low Reynolds numbers and a smooth bed (fine sediment). Some success was achieved in predicting the onset of rolling grain ripples and vortex ripples. Andersen (1999) used a k–ω model coupled with a sediment transport model to simulate self-formed ripples and found that differences in the bed shear stress on fixed and self-formed ripples are not as large as might be expected, although the crest of a self-formed ripple is continuously in motion. Andersen's finding is significant because it indicates that artificial ripples may adequately simulate self-formed ripples. Blondeaux (2001) provided a nice review of vortex ripples. He found that most successful numerical and theoretical analyses have been associated with low Reynolds numbers. For higher Reynolds numbers, direct numerical simulation of vortex ripple behavior is still not practical, but large eddy simulation is promising because large-scale vortices play such a prominent role in ripple development. Blondeaux also suggested that further success in the development of models to predict morphological patterns will occur when additional insights into the mechanisms controlling sediment entrainment and transport are obtained.

Experimental studies of sand ripples are also prevalent. Nakato *et al.* (1977) used a hot-wire anemometer to measure longitudinal and vertical velocities above a rippled sand bed. They focused on sediment concentration and fluxes above the ripples, and presentation of turbulent velocity data was secondary. Nakato *et al.* showed that suspended sediment concentrations were higher above ripple crests than above ripple troughs. Du Toit and Sleath (1981) used a laser Doppler anemometer (LDA) to measure velocities in an oscillatory flow, taking measurements above plane, self-formed rippled, and artificial rippled beds. They showed that, unlike in the outer flow, the streamwise velocity near the crest of the ripple is asymmetric. The peak velocity above the crest occurs when the flow reverses and the vortex that forms on the lee side of the ripple is carried over the crest. As the vortex passes the crest, there is also a peak in the turbulence intensity. Much of the sediment transport over the crest is associated with passage of the vortex. In experiments with high sand concentrations, velocity measurements were not possible. Voropayev *et al.* (1999) measured velocities above a rippled bed with an acoustic Doppler velocimeter (ADV), and obtained results in agreement with those of Du Toit and Sleath (1981).

Sato (1987) and Horikawa and Ikeda (1990) both measured velocities above fixed ripple beds with an LDA, although the crests of the ripples used by Horikawa and Ikeda were sharper than the crests of real vortex ripples. Sato (1987) compared his measurements with results of a k–ε numerical model, and found that the strength of the vortex that develops on the lee side of the ripple greatly influences the production of turbulence and the thickness of the boundary layer. Horikawa and Ikeda (1990) also found that generation of turbulence levels in the flow are correlated to the ripple vortices. They used their results to describe the distribution of kinematic eddy viscosity and the persistence of stationary velocity cells.

With particle image velocimetry (PIV) the entire two-dimensional velocity field above a vortex ripple can be non-intrusively measured at an instant in time. Earnshaw *et al.* (1994) and Earnshaw and Greated (1998) used PIV to measure velocities above ripples made of preformed Styrofoam. They used their measurements to validate a discrete vortex model for predicting vortex trajectories. The absence of suspended sediment prevented interference of the sediment with PIV measurements. Ahmed and Sato (2001) measured velocities above self-formed sand ripples using PIV. They used the 200 μm sand of the vortex ripples as the tracer particles, allowing them to predict onshore volume flux of sediment. Though the sediment fluxes provided by Ahmed and Sato are useful, the relatively coarse, dense sand is not an ideal flow tracer. Furthermore, because of bed reflection, Ahmed and Sato had difficulty measuring velocities near the bed. Recently, PIV was used to measure boundary layer turbulence in the ocean (Nimmo Smith *et al.*, 2002), indicating that it would also be possible to measure velocity fields above ripples in actual coastal settings as long as bed reflections and the presence of suspended sediment are not a problem.

Despite many experimental research efforts, detailed knowledge about velocity fields and sediment transport above ripples is elusive for two primary reasons. First, the presence of suspended sediment makes it difficult to accurately measure velocity because suspended particles can contaminate the measurement device (e.g., hot film anemometers) or bias velocity measurements (e.g., Doppler and image-based velocimetry). Second, the bed is mobile, and placing instruments in the flow affects velocities and sand movement near the bed, ultimately causing measurements with such instruments to be suspect. Moreover, the flow field around moving bedforms is essentially unsteady for sensors attached to a fixed system of reference, thus precluding a simple interpretation of the data. As pointed out, researchers have partially overcome these obstacles by using a fixed bed with the same shape as the ripples. However, measurements above a fixed ripple and a self-formed ripple are not exactly the same since the shape of a self-formed ripple changes slightly with phase, and suspended sediment affects turbulence properties of the flow. Furthermore, fixed ripples cannot self-adjust to compensate for changes in the flow, resulting in error if the ripples and the flow are not adequately matched.

To further the present knowledge about ripple vortices and sediment transport above vortex ripples, an experimental study was conducted in a U-tube at the Ven Te Chow Hydrosystems Laboratory of the University of Illinois at Urbana-Champaign. Results on measurements of the characteristics of the oscillatory flow field above self-formed vortex ripples using PIV with fluorescent tracers for the fluid phase are presented and discussed. The use of fluorescent tracers allowed fluid velocities to be measured in the presence of suspended sediment and adjacent to a moveable bed, providing details about the flow field above self-formed vortex ripples not previously reported. The measurements contribute information about vortex interactions above self-formed vortex ripples, and help clarify the nature of turbulence of the oscillatory flow field in the presence of suspended sediment.

2 Relevant dimensionless parameters

Based on a dimensional analysis, two flow-related dimensionless parameters were chosen to represent the behavior of vortex ripples in an oscillatory flow: the wave Reynolds number and the mobility number (Andersen, 1999). The wave Reynolds number is defined as:

$$\mathrm{Re} = \frac{A^2\omega}{\nu} \tag{1}$$

where, for flow in a U-tube, A is the half stroke of the piston driving the flow, ν is the kinematic viscosity of the water, and ω is the radian frequency of the wave, given by:

$$\omega = \frac{2\pi}{T} \tag{2}$$

where T is the period of oscillation of the flow. The mobility number, ψ, is also useful for characterizing vortex ripples (Nielsen, 1981) and is given as:

$$\psi = \frac{A^2\omega^2}{RgD_{50}} \tag{3}$$

where R is the submerged specific gravity of the bed material (1.65 for quartz sand), g is the gravitational acceleration, and D_{50} is the mean grain size diameter of the bed. Unlike the wave Reynolds number, the mobility number accounts for sediment transport capacity of the oscillatory flow. Many geometric characteristics of vortex ripples are also a function of the mobility number. One other important parameter, a measure of the dimensionless bed shear stress of the oscillatory flow, is the Shields parameter (Nielsen, 1981), $\theta_{2.5}$, and is given by:

$$\theta_{2.5} = \frac{1}{2} f_{\mathrm{w}}\psi \tag{4}$$

where f_{w} is defined by Jonsson (1966) as a wave friction factor.

3 Experimental method

Experiments were conducted in a U-tube (Fig. 2) that was 21-cm wide, 23-cm tall, and 390-cm long. The piston–cam assembly produced an oscillatory flow in the flume, and the piston stroke could be set to 14.6, 18.7, or 22.8 cm by adjusting the linkage between the cam and the piston. The lowest possible oscillation period in the flume was 1.7 s, and the periods investigated in the experiments herein ranged from 1.7 to 2.5 s. Although the flow was not perfectly sinusoidal (Sleath, 1987), the linkage between the cam and the piston was long enough so that the second harmonic of the oscillatory flow was always less than 1% of the fundamental harmonic of the flow. On the side of the flume opposite the piston (Fig. 2), there was a 150-cm long, 30-cm deep bed composed of uniform quartz sand with a mean diameter of 580 μm and a specific gravity of 2.65. Since the flow was not perfectly sinusoidal, the ripples that formed on the bed during experiments migrated very slowly toward the piston. As sand fell into the sand trap (Fig. 2), it was pumped to the opposite side of the sand bed. The maximum current induced in the flume by the pump was estimated by averaging PIV velocity measurements above the ripple crest. The measurements were averaged over the depth and over all phases. The current in the flume was estimated to be less than 3% of the wave amplitude velocity (1 cm/s) for the experiments listed in Table 1.

Based on linear wave theory, flow in the U-tube is similar to the oscillatory flow that occurs near the bed beneath shallow

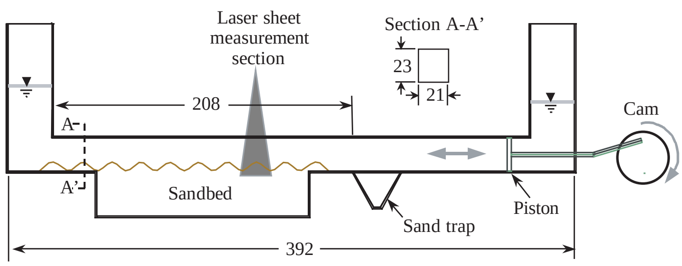

Figure 2 Experimental oscillatory flume (all dimensions in cm).

Table 1 Experiment summary

Run	Piston stroke (cm)	Piston period (s)	Reynolds number, Re	Mobility number, ψ	Shields parameter, $\theta_{2.5}$	Ripple wavelength (cm)	Ripple height (cm)	Image separation (ms)
1	14.6	2.5	1.31×10^4	4.16	0.056	9.2	1.5	7.0
2	14.6	2.0	1.64×10^4	6.51	0.088	9.5	1.3	6.0
3	14.6	1.7	1.93×10^4	9.00	0.122	10.5	1.8	6.0
4	18.7	2.5	2.15×10^4	6.83	0.083	20.0	2.1	3.0
5[a]	18.7	2.0	2.69×10^4	10.67	0.129	13.0	1.8	–
6	18.7	1.7	3.17×10^4	14.77	0.179	13.5	2.3	2.0
7A	22.8	2.5	3.20×10^4	10.15	0.113	17.0	2.4	2.0
7B[a]	22.8	2.5	3.20×10^4	10.15	0.113	21.0	2.4	–
8	22.8	2.0	4.00×10^4	15.86	0.177	22.0	2.6	2.0
9	22.8	1.7	4.71×10^4	21.96	0.244	14.0	2.3	2.0

[a]Geometric characteristics of the vortex ripples were gathered for all of the data sets shown in the table, but for Experiments 5 and 7B no PIV data are available.

progressive waves, but there are two differences (Fredsøe and Deigaard, 1992; Nielsen, 1992). First, progressive waves produce elliptical flow motion in the water column above the bed, but the U-tube only reproduces the streamwise component of the elliptical motion. Second, in the U-tube the instantaneous flow fields above two adjacent equilibrium ripples are exactly the same, whereas beneath progressive waves the flow fields are different because the elevation of the water surface above the two ripples is different. For progressive waves with wavelengths that are large relative to the depth, the vertical component of the elliptical motion is negligible near the bed, and therefore should not affect the flow field in the vicinity of the vortex ripples (Jonsson and Carlsen, 1976). Furthermore, as long as the wavelength of the surface waves is significantly greater than the wavelength of the vortex ripples, the difference between the instantaneous flow fields above adjacent ripples will be insignificant. Consequently, both differences between the two types of oscillatory flow are considered to have a secondary impact on the production of vortex ripples (Nielsen, 1992).

At the beginning of each experiment, the U-tube was operated for several hours until the ripples reached what was perceived to be their fully developed, equilibrium amplitude state. To ensure that the ripples had reached an equilibrium state, the U-tube was allowed to operate for several more hours before measurements were taken. Smith and Sleath (2005) estimated the number of cycles required for vortex ripples to change from one equilibrium state to another for flow conditions similar to those given in Table 1. For all of their experiments, fewer than 800 cycles were required for transient ripples to make 80% of the adjustment from initial height to equilibrium height. In comparison, the data sets identified in Table 1 were collected after thousands of cycles.

Particle image velocimetry was applied to measure the flow field above vortex ripples in the U-tube. A 120 mJ double-pulsed Nd:YAG laser was used to illuminate a thin cross-section of the flow field as shown in Fig. 2. Image pairs were captured using an 8-bit, 1000 by 1016 pixel digital camera. The camera had a 50-mm lens and was synchronized with the laser. The size of the capture field was about 20-cm by 20-cm.

Fluorescent tracer particles (75 μm) were used to optically discriminate between water and sediment motion, because sand and water velocities were not the same. Fluorescent tracers have been used to separate phases in a number of multiphase flows (e.g., Hassan *et al*., 1993; Kiger and Pan, 2000; Deen *et al*., 2002), but many of these studies have been of gas–liquid mixtures. According to Deen *et al*. (2002), it may be possible to apply the technique in areas with sediment concentrations as high as 4% by volume. The tracers used in this investigation were made of a Melamine resin-based polymer and were manufactured by Dantec. The fluorescent coating on the tracers, Rhodamine B, had a peak excitation wavelength of 550 nm and a peak emission wavelength of 590 nm. A 532-nm Nd:YAG laser was used to excite the tracers, and a 540-nm high-pass optical filter prevented the camera from capturing anything except tracer emissions (García *et al*., 2002). The filter also removed light reflected from the boundaries that would otherwise have interfered with near-bed measurements. Figure 3 shows a PIV image with and without optical filtering.

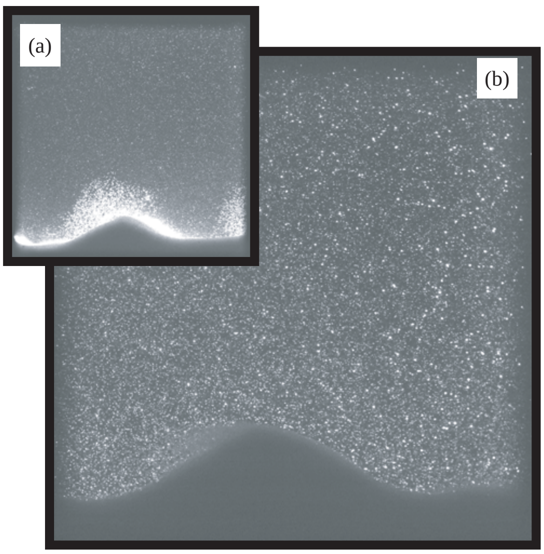

Figure 3 Comparison of (a) unfiltered and (b) optically filtered PIV images.

Without filtering, the sediment causes considerable interference, demonstrating the advantage of using fluorescent particles.

The tracers were relatively large, but the specific gravity of the tracers was only 1.5. In order to assess the frequency response of the tracers, equations of particle motion presented by Mei (1996) were numerically solved. In the simulation, a tracer particle was subjected to a one-dimensional sinusoidal flow with a peak velocity of 40 cm/s—the highest velocity tested in the U-tube. Results showed that the trajectory of a tracer particle was within 5% of the trajectory of the flow for frequencies as high as 270 Hz. In contrast, 580 μm sand, subjected to the same criteria, could only follow flow oscillations with frequencies as high as 2 Hz. Based on these results, it was concluded that the response of the tracer particles was acceptable.

Nine experiments were conducted in the U-tube, each with a different combination of wave amplitude and period (Table 1). Wave Reynolds numbers of the experiments ranged between 13,000 and 47,000, and mobility numbers ranged between 4 and 22. For each experiment, 3600 image pairs were collected—300 pairs per phase for 12 equally spaced phases. The time that elapsed between the two images of an image pair (separation time) was adjusted for each experiment to optimize PIV data quality. Within each experiment, a constant separation time was used. Although increasing the separation time for phases with low velocities would have improved accuracy, the presence of large vortices caused some regions of the flow field to have high velocities for all of the phases.

Since the sand ripples were not completely stationary, PIV images were adjusted so that velocity vectors could be properly phase-averaged. This was accomplished by analyzing the PIV data using a moving Cartesian coordinate system with the origin at the ripple crest. Pictures were only taken when a sand ripple was near the center of the field of view of the camera. All of the images in an experiment were then aligned as shown in Fig. 4. Vertical rows of pixels along the edges of the images were clipped so that the ripple crest was centered in the image for all realizations (within a few pixels). The accuracy of the alignment procedure was assessed for each experiment, by superimposing tracer images from all of the realizations onto one composite image. In the composite image, the area occupied by the ripple was void of tracers, and the flow area had a high density of tracers. Between the two areas was a narrow region where the concentration of tracers was neither high nor zero; this region was the consequence of inexact ripple alignment. The region was approximately 10 pixels thick in the worst case, indicating an alignment uncertainty of less than 2 mm.

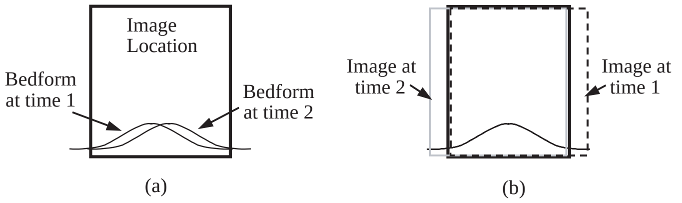

Figure 4 Image correction procedure: (a) superposition of two images before alignment and (b) after alignment.

Velocity fields were calculated using Insight 3.0 software by TSI, Inc. The PIV algorithm consisted of an fast Fourier transform (FFT)-based cross-correlation method applied to subwindows (interrogation areas) that were 64 $\times$ 64 pixels in size. Velocity vectors significantly higher than the amplitude velocity or significantly different from the mean of the four neighboring vectors were rejected. Care was taken to capture high quality images, but approximately 5% of the vectors collected were erroneous—primarily due to high sand concentrations. Of the erroneous vectors, approximately half were replaced with the mean of the four neighboring vectors; the remaining half could not be interpolated and were excluded from calculations. No frame of reference adjustments were made to the velocities since it was not clear which reference frame was best (stationary or moving with the ripples). However, the ripples migrated very slowly ($<$0.3 mm/s for all experiments), and differences between the two possible reference frames were insignificant. Following the filtering process, the vectors were phase-averaged. Moving averages of phase-averaged velocities were examined to determine if 300 image pairs provided statistically representative ensemble averages. Over 95% of the phase-averaged velocities examined were within 5% of their final values when only half of the image pairs were used to compute the averages. Of the few velocities that did not converge as rapidly, most were in places where sand concentrations were very high or a substantial portion of the interrogation area was not in the flow region. In these locations, some image pairs did not yield valid velocities, reducing the number of vectors included in the corresponding phase average. However, for most of the flow field and for all phases, 300 image pairs were sufficient. Phase-averaged vorticity was calculated from the velocity fields using a central difference scheme. Vorticity was only determined in locations where all four neighboring velocity vectors were valid. Finally, the velocity fields were also used to calculate turbulence statistics.

4 Data quality considerations

There are two sources of error associated with instantaneous PIV measurements: separation time error and particle displacement error. The Nd:YAG laser has a combined pulse width and jitter of less than 10 ns, and separation times are on the order of milliseconds. Thus, as pointed out by Adrian (1986), separation time error is insignificant. Displacement errors are influenced by distortion of the object field, camera resolution, seed particle concentration, and seed particle size. The previously specified resolution and magnification of the camera result in pixel sizes of about 0.2 mm by 0.2 mm, dimensions that are more than twice the mean tracer diameter. Even so, it can be shown that mean-sized tracers will straddle multiple pixels more than 60% of the time. Light diffraction and variations in particle size and shape also increase the effective size of particle images. Median particle image sizes measured directly from the PIV images were typically 2–3 pixels—similar to optimal sizes prescribed by Prasad *et al.* (1992) and Cowen and Monismith (1997). Interrogation areas with a fixed size of 64 $\times$ 64 pixels and 75% overlap were used, and the spatial resolution was between 2.2 and 3.3 mm, depending on the experiment, tracer counts being between 30 and 50 particles per interrogation area. As described previously, all of the realizations belonging to an experiment had the same separation times (Table 1). A Gaussian bi-directional curve fit was used to achieve sub-pixel accuracy, and accuracy may be better than 0.1 pixels (see Willert and Gharib, 1991; Westerweel, 1993). A fixed distance-to-pixel ratio was used to calculate displacements for each experiment. Because of slight changes in camera location between experiments, this ratio was reassessed for each experiment. Pictures of a 1 cm by 1 cm grid placed in the object field revealed that the distance-to-pixel ratio was constant over the entire image field. The distance-to-pixel ratio was estimated to have a relative accuracy on the order of 1%. Based on the assumptions given above, the measurement uncertainty of instantaneous velocities is about 0.5 cm/s for the current set of experiments.

In unsteady, non-uniform flows, some additional error is introduced when quantities are ensemble-averaged because the positions and phases at which individual realizations are gathered are inexact. Phase uncertainty is a result of timing errors associated with the triggering mechanism. Using an oscilloscope, the photodetector trigger signal was found to have a maximum phase error of only 0.2% (0.75°), caused primarily by cam vibration. Position uncertainty is a result of the necessary realignment of the images because of ripple migration. While realignment of the images does not affect the accuracy of instantaneous velocities, it does result in error for the ensemble-averaged quantities. Uncertainty of the location of interrogation areas is estimated to be 5 pixels (∼1 mm). The effect of these uncertainties on phase-averaged velocity and vorticity was determined by doing a multi-sample uncertainty analysis.

The uncertainties of estimated phase-averaged velocities were found by calculating the variances of the average velocities (Moffat, 1988; Benedict and Guild, 1996). Using this method, typical 95% confidence intervals of the velocity were ±0.1 cm/s over most of the velocity field. In a few locations, mostly close to the bed, where interference reduced the number of valid realizations, the 95% confidence interval was occasionally as large as ±1 cm/s. In comparison, amplitude velocities of the current set of experiments range from 18 to 42 cm/s.

Using the root-sum-square (RSS) technique described by Kline and McClintock (1953), uncertainties of the phase-averaged vorticity field were also determined. These uncertainties were a function of the uncertainties of the phase-averaged velocity field and the spacing between interrogation areas (see Liu *et al*., 2004). Typical 95% confidence intervals of the average vorticity were $\pm 0.25\,\mathrm{s}^{-1}$, while maximum 95% confidence intervals were on the order of $\pm 3\,\mathrm{s}^{-1}$. Based on these measurement uncertainties, the relative uncertainties of calculated phase-averaged vorticities were observed to be very high except in the vicinity of strong vortices (i.e., within the vortices that form behind the sand ripples and that are transported between the ripples by the flow). Within these vortices, the relative uncertainty of the phase-averaged vorticity was generally between 10 and 40%.

5 Ripple geometry

Vortex ripple geometry is a function of the oscillation amplitude. For a given wave and sediment size, ripples generally form at a specific wavelength, although secondary ripple wavelength modes are sometimes present. As long as the amount of sediment suspended from the tops of the ripples remains low, the wavelength at which the ripples form is directly related to the amplitude of the oscillatory flow (Sleath, 1984). The wavelength of the vortex ripples is less than twice the amplitude of the flow and is a fixed fraction of the amplitude for a significant range of flows (Nielsen, 1981, 1992).

Table 1 shows flow and geometric characteristics of the fully developed, equilibrium amplitude vortex ripples, including ripple wavelength and height, mobility number, Reynolds number, and Shields parameter. Ripple wavelength and height were measured in the experimental section of the flume using a ruler. For each test, wavelength and height were measured for three ripples; Table 1 shows the averaged results. The estimated measurement uncertainty of the ripple wavelength and height is 2 mm. This corresponds to maximum relative uncertainties of 2 and 15% for the ripple wavelength and height, respectively. The ripple height, η, scales well with the flow amplitude as shown in Fig. 5(a). The ratio η/A remains approximately constant with a value of about 0.2, independent of the experimental conditions. The ratio of ripple height to ripple wavelength, λ, is plotted against the Shields parameter in Fig. 5(b), and is in agreement with the equation presented by Nielsen (1981). The ratio ranges from 0.1 to 0.2 and is approximately independent of the Shields parameter. When the mobility number is less than 20, the dimensionless ripple wavelength λ/A is expected to be about 1.33 (Nielsen, 1981), and all of the experiments have mobility numbers less than 20, except Experiment 9 for which the mobility number is slightly greater than 20. The dimensionless ripple wavelengths are close to the expected value of 1.33 for most of the experiments (Fig. 5c). In Fig. 5(d), the dimensionless ripple wavelengths are plotted alongside a curve fit of historical data given by Nielsen (1981). The scatter of the present data about the curve fit is consistent with the scatter of historical data. A closer inspection, however, reveals that there are three experiments (4, 7b and 8, see Table 1) for which the ratio λ/A is higher than in the other experiments and closer to about 2.0. This appears to be related to the behavior of the vorticity of the flow and is analyzed in more detail in the next section.

The PIV images were used to assess how much ripple shape changed with phase. For each phase, tracers from all of the aligned images were superimposed onto one image, revealing the phase-dependent outline of the sand ripple. For Experiment 9, the flow with the highest Reynolds number, variation of the ripple height was not measurable for any of the phase-dependent ripple outlines. The crest of the ripple did lean slightly in the direction of the mean velocity, but the phase-averaged horizontal displacement of the crest from the center of the ripple was less than 0.5 cm over all phases. Crest motion was even less for experiments with smaller Reynolds numbers. These results confirm

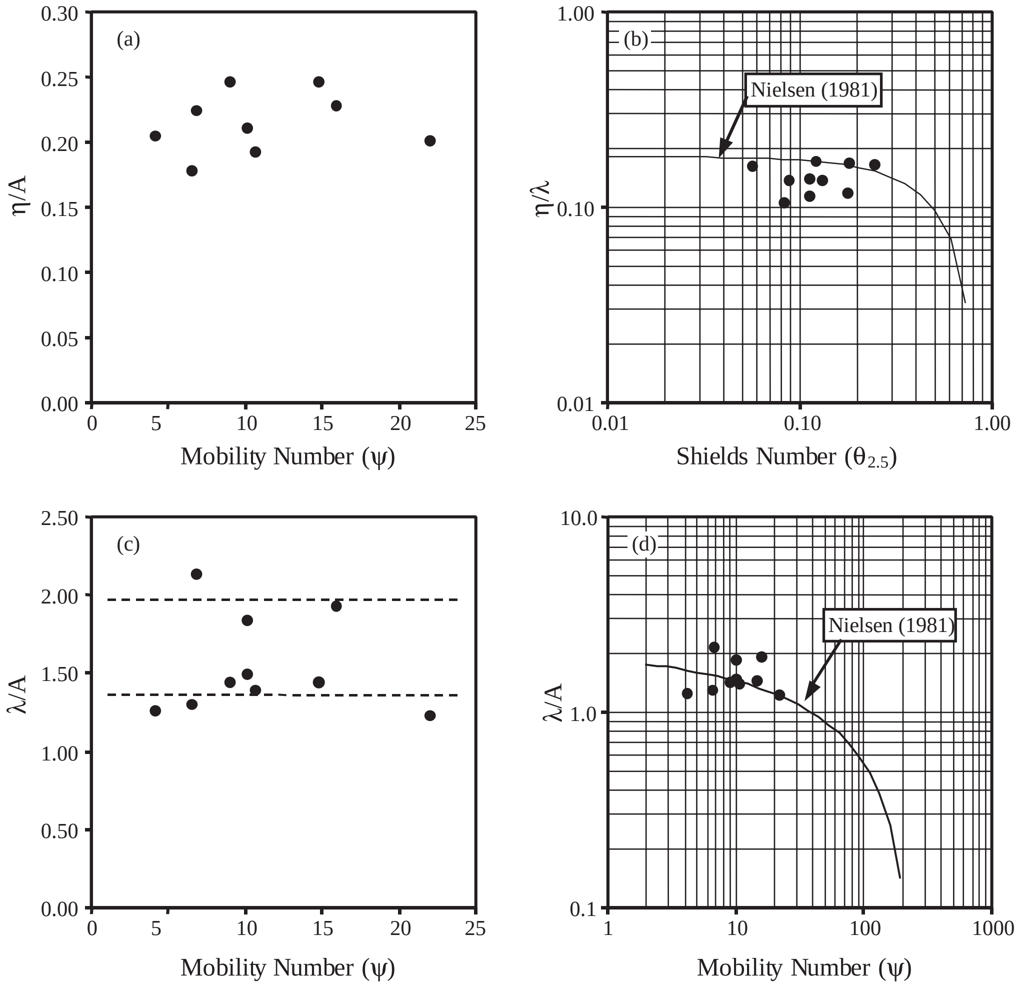

Figure 5 (a) Ratio of ripple height and flow amplitude as a function of the mobility number; (b) ratio of ripple height and wavelength as a function of the Shields parameter; (c) ratio of ripple wavelength and flow amplitude as a function of the mobility number; dashed lines represent average values for the corresponding group of data points; and (d) dimensionless ripple wavelength as a function of the mobility number; comparison with Nielsen's (1981) model.

Andersen's (1999) similar conclusion obtained from numerical simulations.

6 Vortex dynamics

Vortex motion strongly influences geometric characteristics of the vortex ripples. Not only is the circulation strength of the vortex that develops on the lee side of the ripple responsible for the shape and size of the ripple, but also subsequent advective transport of the associated vorticity and energy content is strongly related to the spacing of the ripples. The individual vortices that form on the ripples vary from oscillation to oscillation, having slightly different strengths and trajectories. Phase-averaged values of these properties are presented in this section. In this paper, each time a vortex is mentioned, we are alluding to the phase-averaged vortex.

Phase-averaged PIV velocity fields were calculated for 12 phases of each of the experiments in Table 1. All velocities were made dimensionless by scaling them with the amplitude velocity, ωA. There were some interrogation areas immediately above the bed for which velocities could not be calculated. The missing data occurred in locations where very high concentrations of sediment periodically blocked the view of the camera, primarily in a small region on the lee side of the crest when the flow reached its peak velocity. There was also loss of velocity data when most of an interrogation area was occupied by the bed, reducing the effective size of the interrogation area, and resulting in poor correlation.

Examples of the dimensionless vorticity fields associated with the measured velocities are shown in Figs 6 and 7 (for Experiments 7 and 9, respectively). Vorticities were made dimensionless by scaling them with ω. Experiments 7 and 9 have the same flow amplitude, but Experiment 7 has a longer period than Experiment 9. There are two primary vortex structures in each case, one with positive rotation (counterclockwise in Figs 6 and 7) and one with negative rotation (clockwise in Figs 6 and 7). Vortex evolution is depicted in these figures. Note that as a vortex leaves one side of the image, its counterpart from an upstream ripple appears on the opposite side of the image. Since the wavelength of the sand ripples is known, the counterpart can be used to track the trajectory and strength of the vortex even after the original vortex leaves the imaging area. Negative vortices are tracked in Figs 6 and 7 by numbering the sequential positions of the vortices.

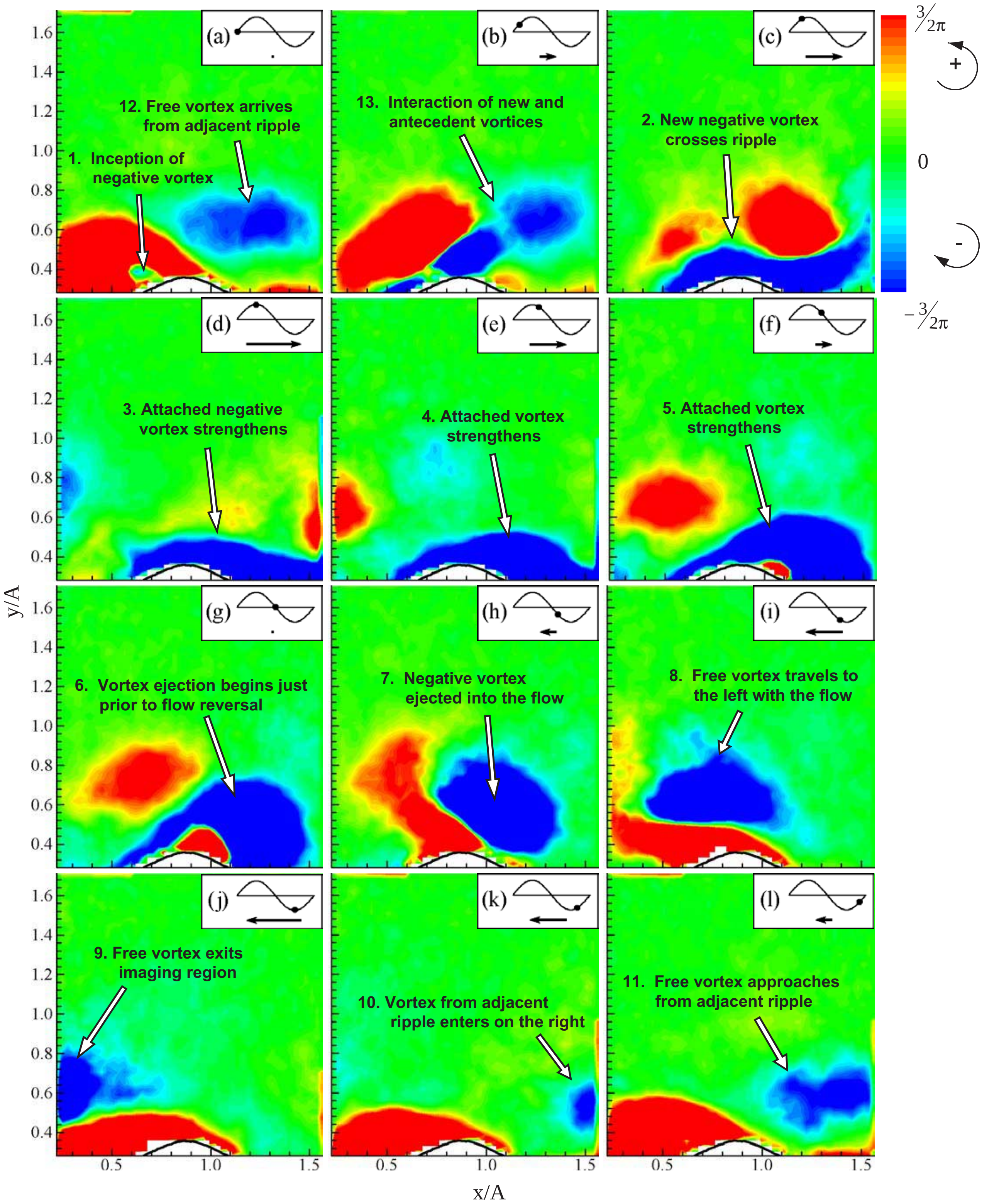

Figure 6 Contour plots of dimensionless vorticity as a function of phase for Experiment 7. Scale and sign convention is given in the upper right hand corner. Mean flow direction is shown for each phase.

The negative vortex originates near the bed on the left side of the ripple. This vortex is created as the strong, positive vortex that developed in the separation zone during the previous half-period is ejected from the bed (e.g., Fig. 7b, phase $\pi/6$). As shown by the attached negative vortex in Figs 6(f) and 7(f), the ejection of vortices can begin prior to flow reversal. Villard and Osborne (2002) attributed this behavior to a phase lead of the flow near the bed. Consequently, inception of a new vortex may also occur prior to flow reversal. After this, the vortex crosses the ripple crest to the downstream side of the ripple where, due to flow separation, it increases in strength and size, particularly as the flow decelerates towards phase π (e.g., Fig. 7c–g, phases $\pi/3$ to π). Then the vortex is ejected and dissipates after the flow reverses directions, passing over and moving away from the ripple on which it was

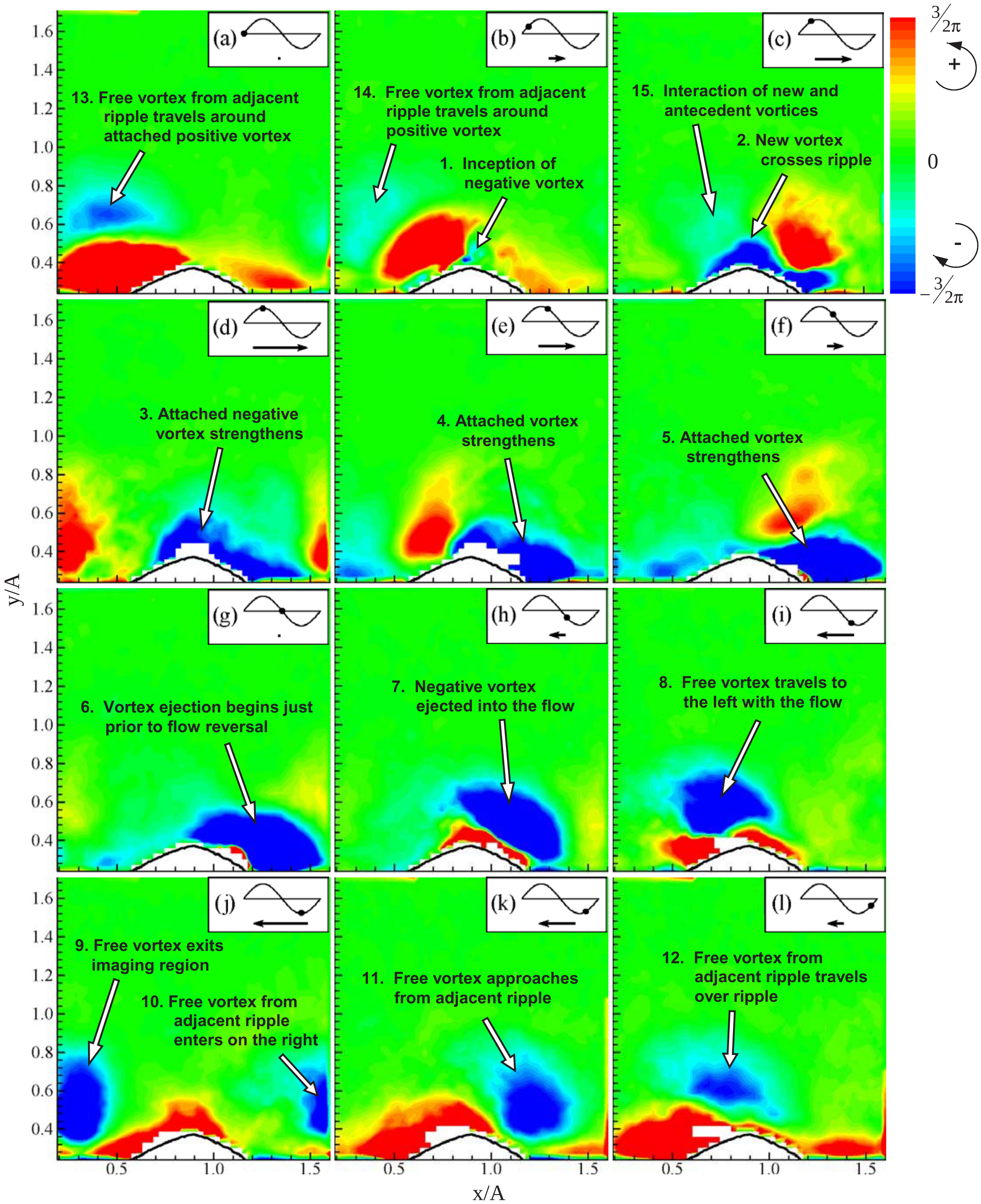

Figure 7 Contour plots of dimensionless vorticity as a function of phase for Experiment 9. Scale and sign convention is given in the upper right hand corner. Mean flow direction is shown for each phase.

formed (e.g., Fig. 7a, b, e–l phases, $7\pi/6$ to $13\pi/6$). As suggested by Villard and Osborne (2002), when the vortex gets close to the neighboring ripple, it interacts with the local positive vortex and the newly formed negative vortex (e.g., Fig. 7a, l, phases $11\pi/6$ and 2π). It is hypothesized that this interaction determines the ripple wavelength. For example, if adjacent ripples are separated by less than one equilibrium wavelength, an imbalance in the transfer of vorticity between the ripples leads to asymmetry of the sediment transport on the sides of the ripples, an imbalance that causes the ripples to spread apart. This mechanism is discussed in more detail below. The fact that the separation vortex is created on the upstream side of the bedform is in contradiction with some previous investigations, which identify its location of origin in the lee zone (e.g., Earnshaw and Greated, 1998).

Although subtle differences exist, the observed vortex behavior was similar for all experimental conditions.

Earnshaw and Greated (1998) presented experimental information about vortex dynamics above artificial vortex ripples for four oscillatory flows. Their vortex ripples had a fixed wavelength of 22 cm for all four tests. Similar information is presented herein, but in contrast to the work of Earnshaw and Greated, the results presented are for self-formed ripples with wavelengths ranging from 9 to 22 cm. Following the method described by Earnshaw and Greated, vortex strength was defined using the circulation of all of the cells that were identified as part of the vortex:

$$\Gamma = \sum_i \omega_{vi} A_i \tag{5}$$

where Γ is the vortex circulation, ω_{vi} is the vorticity in an area belonging to the defined vortex region, and A_i is the area associated with ω_{vi}. The product $\omega_{vi} A_i$ is summed over the entire extent of the vortex. Circulation was made dimensionless by scaling it with $A^2\omega$.

The x component of the center of the vortex, x_c, was found using the equation:

$$x_c = \frac{\sum_i \omega_{vi} A_i x_i}{\sum_i \omega_{vi} A_i} = \frac{\sum_i \omega_{vi} x_i}{\sum_i \omega_{vi}} \tag{6}$$

where x_i is the x location of each interrogation area within the extent of the vortex. In Eq. (6) the center of the vortex is weighted toward the location of maximum vorticity. A similar equation is used to find the y component of the vortex center. The location of the vortex center is given relative to the crest of the ripple on which the vortex formed (i.e., the origin is at the crest of the ripple on which the vortex formed). While the relative uncertainties of the vorticities calculated within each vortex are fairly high, they do not greatly affect determination of the centroid of the vortex because variation of vorticity within each vortex is strong. It is estimated that the location of each vortex has an uncertainty of less than 1 cm.

The extent of the vortex was defined as the region that included all of the contiguous interrogation areas that had a vorticity of at least 10% of the maximum vorticity within the vortex (see Earnshaw and Greated, 1998). In the present case, the 10% boundary worked adequately when the vortex first formed, but as the vortex weakened, the extent of the vortex was not as well defined, and the method sometimes identified the wrong centroid. Consequently, 50% of the maximum vorticity was used to define the extent of the vortex region for determining the vortex centroid. In regions where the 10% boundary was well defined it was found that there was very little difference between the centroids calculated using the 10 and 50% criteria. The circulation was always found based on the 10% criteria so that it would not be underestimated, but some data points were rejected when the method returned the wrong vortex (this was easily discerned using images like those shown in Figs 6 and 7). The dimensionless circulation based on the 10% criteria is subsequently referred to as Γ_{90}. Additional points were discarded if the vortex was cut off by the edge of the image, and as noted by Earnshaw and Greated, near-bed measurements of circulation were not particularly accurate because the PIV interrogation areas have a finite size and cannot be made to fit the bed profile exactly. Thus, circulation measurements are more accurate for a free vortex than for one that is attached to a sand ripple. The RSS method showed that the relative uncertainty of the circulation was most strongly affected by the uncertainties of the largest calculated vorticities within the defined vortex region. These vorticities also had the lowest relative uncertainties. Based on the analysis it was estimated that relative uncertainties of circulations are typically less than 10%, though this estimate is less rigorous than the uncertainties cited for phase-averaged velocity and vorticity because of the difficulties associated with identifying the exact boundaries of the vortex.

Trajectories of the vortices were found for all of the experiments, and a representative subset of the trajectories is shown in Fig. 8; the trajectories shown are those of Experiments 7 and 9

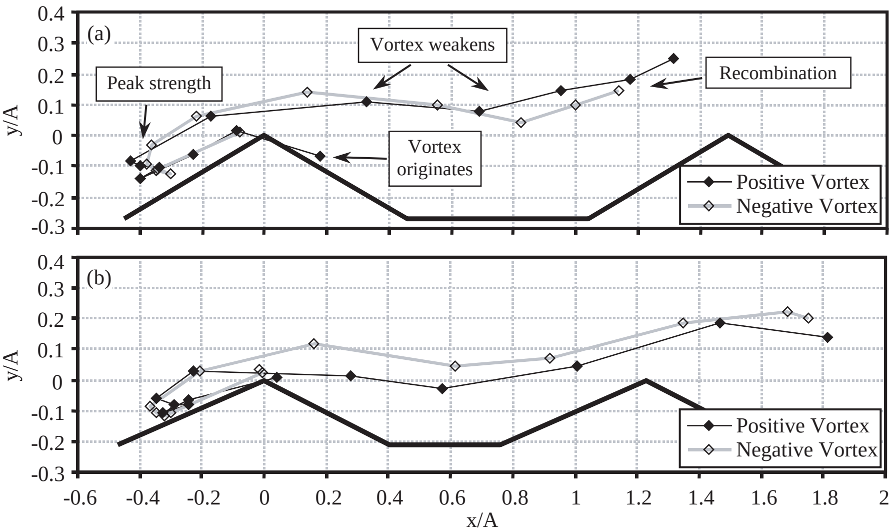

Figure 8 Vortex trajectories for (a) Experiment 7 and (b) Experiment 9. (a) Also shows where the vortex originates, gains peak strength, weakens, and recombines with the new vortex on an adjacent ripple. For each experiment the sign of the x component of the negative vortex has been changed to facilitate comparison with the corresponding positive vortex.

(the mirror image of the trajectory of the negative vortex is used so that trajectories of the positive and negative vortices can easily be compared). Vortices in Experiment 7 travel about 0.9 ripple wavelengths from the ripples on which they formed, but in Experiment 9 the vortices travel about 1.5 ripple wavelengths. This significant difference in vortex behavior for Experiments 7 and 9 also appears in Figs 6 and 7. In both cases, a free vortex that formed on an adjacent ripple during the previous cycle can be observed interacting with a newly formed vortex of the same sign (e.g., Figs 6b and 7c). However, in Experiment 9, the free vortex travels around an attached vortex of opposite sign before interacting with the newly formed vortex. These observations mark a clear difference with respect to those made in the artificial ripple experiments by Earnshaw and Greated (1998). In those experiments vortices had excursions of two or more wavelengths. It is unlikely that for equilibrium bedform conditions the vortices could travel two ripple wavelengths since the vortices are advected by the mean flow which has an excursion of $2A$, comparable or only slightly larger than one ripple wavelength (Fig. 5c).

The ratio between the extent of the vortex excursion, x_T, and the ripple wavelength is plotted in Fig. 9 for different experimental conditions. It is clear that this ratio has approximate values of either 0.8 or 1.5, independent of the experimental conditions. On the other hand, x_T seems to scale well with the piston stroke ($2A$), such that the ratio $x_T/(2A)$ is about 0.9, independent of the experimental conditions (Fig. 10). Thus, the vortices are advected by the mean oscillatory flow and simply follow, in their horizontal excursions, the trajectory of the piston. The ripples seem to adjust their wavelength to the vortex excursions, but two possible states are defined for the same flow condition, as indicated previously: either a long wavelength, comparable to x_T and the piston stroke, or a short wavelength of about 70% of the piston stroke (Fig. 5c, where Experiments 7a and 7b are a good example of this dual behavior). In the former case, vortex recombination occurs between ripples, thus pushing the ripples apart, while in the latter case it occurs on the opposite side of the neighboring ripple (with respect to the ripple on which the vortex was first created), thus pushing the ripples together (Fig. 8). For both possible

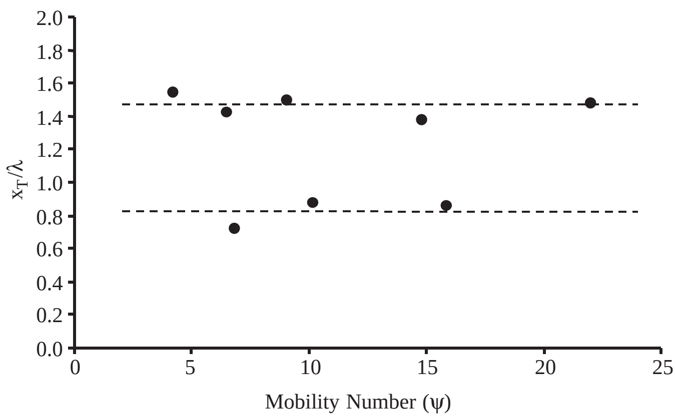

Figure 9 Horizontal extension of the vortex excursion made dimensionless with ripple wavelength as a function of the mobility number. Dashed lines show the average dimensionless value of the two possible vortex excursions.

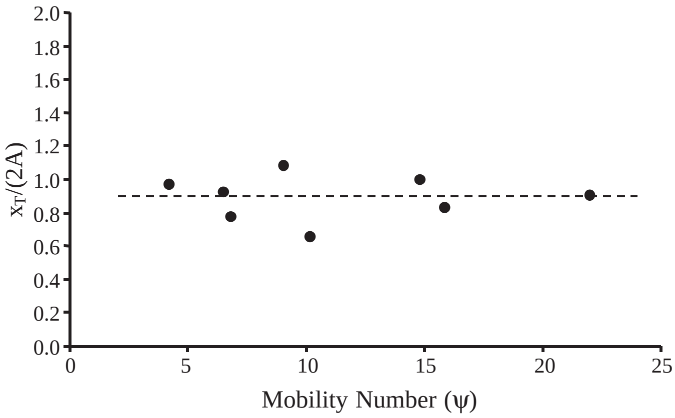

Figure 10 Horizontal extension of the vortex excursion made dimensionless with flow stroke as a function of the mobility number. The dashed line represents the average dimensionless value of the vortex excursion.

wavelengths the ripple height remains invariant (Fig. 5a). These two possible states for ripples generated under similar experimental conditions seem to be indicative of a hysteresis phenomenon, possibly generated by the manner in which the present experiments were conducted. In general, the bed was not started flat in every experiment. In most cases, the ripples were allowed to evolve from one finite amplitude state to another, as they would in nature, simply establishing a new set of experimental conditions and letting the bed adjust to these new conditions. The wavelength selected may have been dictated by the previous bed deformation, depending on the ability of the advected vortices to recombine on one side or the other of the evolving ripples. Care was taken to make sure the ripples reached an equilibrium state, but it later became apparent that initial conditions were also important. In retrospect, starting each experiment with a flat bed would have been better experimental procedure, but most natural ripples do not begin this way, and starting with a flat bed may have eliminated the evidence of hysteresis. If correct, this theory would help to explain some of the scatter associated with previously reported ripple geometries (Nielsen, 1981, 1992). Evidence for hysteresis of vortex ripples systems has also been reported by Traykovski *et al.* (1999), but, undoubtedly, this phenomenon needs to be studied in more detail.

Γ_{90} was measured as a function of phase for each vortex. With few exceptions, the circulations measured for the positive and negative vortices at corresponding phases had similar magnitudes. The dimensionless circulations of the two vortices were averaged (after phase-shifting the positive vortex). Figure 11 shows the average dimensionless vortex circulation, normalized using its maximum value, Γ_{90p}, versus phase for each experiment. Although the peak velocity of the flow occurs at $\pi/2$ radians, the peak circulation usually occurs just prior to flow reversal (π radians). Thus, the vortices continue to gain strength even after the flow begins to decelerate; furthermore, the rate of strength gain is higher during this stage. As discussed previously, at the end of the oscillation period the circulation of the vortex is not entirely dissipated, but the amount of residual circulation left for the final stage prior to recombination is about 10% of the peak value (Fig. 11).

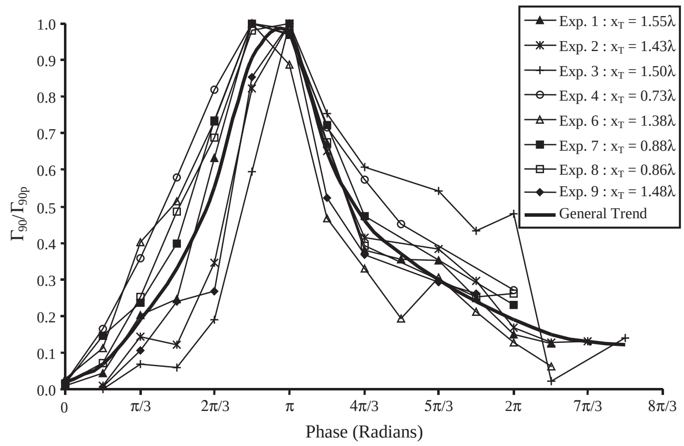

Figure 11 Dimensionless vortex circulation (Γ_{90}) normalized with its peak value (Γ_{90p}) as a function of phase for each experiment. The solid line shows the general trend of the data.

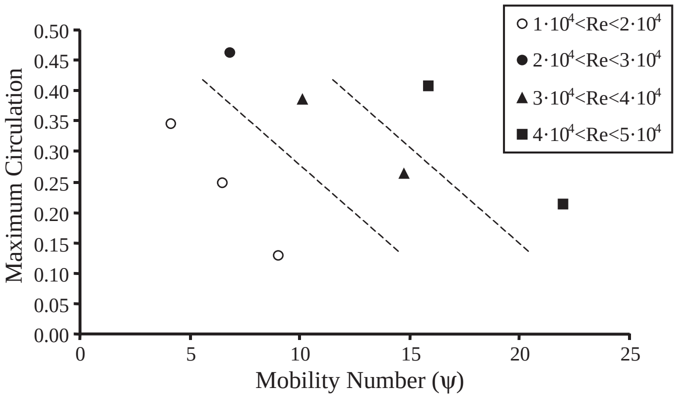

Figure 12 Peak dimensionless circulation Γ_{90p} as a function of the mobility number. Data points are grouped according to similar values of Re.

The dimensionless peak circulation, Γ_{90p}, tends to increase as the Reynolds number of the oscillatory flow increases and to decrease as the mobility parameter increases (Fig. 12). Similar behavior was observed for the turbulent kinetic energy of the flow. The reason why peak circulation decreases as the mobility parameter increases could not be determined from the present data set, but possible explanations include: (1) changes in ripple geometry reduce form drag, decreasing production of vorticity and turbulent kinetic energy, or (2) enhanced sediment concentrations associated with higher mobility numbers dissipate more energy.

Figure 13 shows ripple height and wavelength as a function of the vortex circulation at phases of $5\pi/6$ and π, and underscores the importance of vortex strength. Both the height and the wavelength clearly increase with vortex strength. While a vortex is attached to a ripple, it pushes sand (as bed load) up the side of the ripple toward the crest. Vortices that form on alternate sides of the ripple are responsible for development of the ripple, and if the vortices have greater circulation, they are capable of pushing the sand higher and they produce larger ripples. This suggests a different scaling for the circulation. In fact, if the local scale $\lambda\eta\omega$ is used to scale the peak circulation instead of $A^2\omega$, it is found

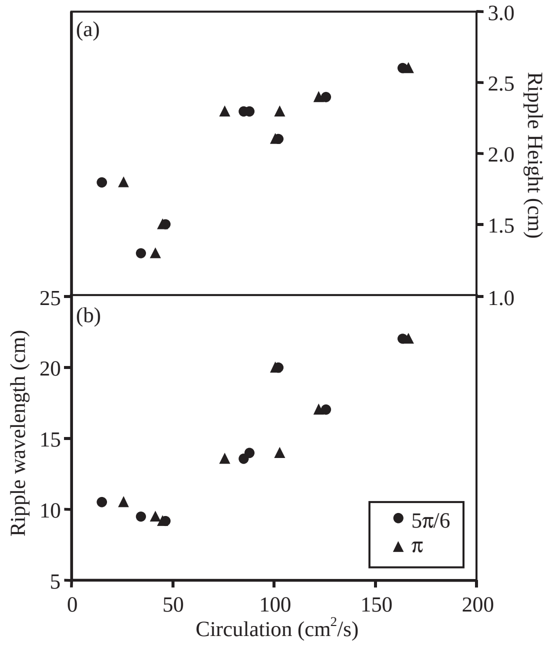

Figure 13 (a) Ripple height and (b) ripple wavelength as a function of vortex circulation for phases of $5\pi/6$ and π.

that most dimensionless peak circulations calculated using the present experimental results have a magnitude close to 1 and in the range from 0.8 to 1.2.

7 Conclusions

Use of fluorescent tracer particles made it possible to measure flow velocities above self-formed vortex ripples in the presence of suspended sediment. These measurements provided information on ripple geometry and flow structure. Ripple height scales well with the flow amplitude so the ratio η/A remains approximately constant, with a value of about 0.2, independent of the experimental conditions. The ratio of ripple height to wavelength is also approximately constant, with values of about 0.1–0.2. The dimensionless ripple wavelength λ/A is close to 1.36 for most of the experiments, but this ratio can be higher in certain experiments and closer to about 2.0, which appears to be the result of a hysteresis phenomenon associated with the transport of vorticity in the system. Vortices that develop in the lee side of the ripples and are advected by the oscillatory flow play a major role in the mechanisms leading to finite amplitude bedforms. Coupling between flow and sediment transport processes determines the circulation strength of these vortices as well as the shape and size of the ripples. Subsequent advective transport of flow vorticity and energy determines the spacing of the ripples. Vortices generated on one ripple (ripple A) during a particular oscillation recombine with newly formed vortices in the neighboring ripple (ripple B) at the beginning of the next oscillation. Two possible states for similar flow conditions were observed, indicating a hysteresis: vortex recombination occurs either in the space between ripples A and B or on the far side of ripple B. In the former case the ripple wavelength tends to be higher than in the latter. For a given experimental condition, the initial bed relief may influence the selection of one state or the other, but this has not been proven. The peak circulation of the vortices usually occurs just prior to flow reversal, implying that the vortices continue to gain strength even after the flow begins to decelerate. The dimensionless peak circulation, Γ_{90p}, tends to increase as the Reynolds number of the oscillatory flow increases and to decrease as the mobility parameter increases.

Acknowledgments

The authors would like to thank the Coastal Geosciences Program of the Office of Naval Research for their financial support of this project under Grants N00014-01-1-0337 and N00014-05-1-0083 to the University of Illinois at Urbana-Champaign.

Notation

A = Wave amplitude
D_{50} = Mean grain size diameter of bed sediment
f_w = Wave friction factor
g = Gravitational acceleration
R = Submerged specific gravity
Re = Wave Reynolds number
T = Period of wave oscillation
x = Streamwise distance from the ripple crest
x_c = Streamwise location of the vortex center
x_T = Streamwise extent of vortex excursion
y = Vertical location
y_c = Vertical location of the vortex center
Γ = Vortex circulation
Γ_{90} = Finite representation of vortex circulation
Γ_{90p} = Peak value of vortex circulation
η = Ripple height
λ = Ripple wavelength
ν = Kinematic viscosity
$\theta_{2.5}$ = Shields parameter
ψ = Wave mobility number
ω = Radian wave frequency
ω_ν = Vorticity

References

1. ADRIAN, R.J. (1986). "Multi-point Optical Measurements of Simultaneous Vectors in Unsteady Flow—A Review". *Int. J. Heat Fluid Flow* 7(2), 127–145.
2. AHMED, A.S.M. and SATO, S. (2001). "Investigation of Bottom Boundary Layer Dynamics of Movable Bed by Using Enhanced PIV Technique". *Coastal Engng. J.* 43(4), 239–258.
3. ANDERSEN, K.H. (1999). "The Dynamics of Ripples Beneath Surface Waves and Topics in Shell Models of Turbulence". PhD Thesis, University of Copenhagen, Copenhagen.
4. ARDHUIN, F., DRAKE, T.G. and HERBERS, T.H.C. (2002). "Observations of Wave-generated Vortex Ripples on the North Carolina Continental Shelf". *J. Geophys. Res.* 107(C10), 3143, doi:10.1029/2001JC000986.
5. AYRTON, H. (1910). "The Origin and Growth of Ripple-mark". *Proc. Roy. Soc. London* A84(571), 285–310.
6. BAGNOLD, R.A. (1946). "Motion of Waves in Shallow Water, Interaction between Waves and Sand Bottoms". *Proc. Roy. Soc. London* A187, 1–15.
7. BENEDICT, L.H. and GUILD, R.D. (1996). "Towards Better Uncertainty Estimates for Turbulence Statistics". *Exp. Fluids* 22, 129–136.
8. BLONDEAUX, P. (1990). "Sand Ripples Under Sea Waves. Part 1. Ripple Formation". *J. Fluid Mech.* 218, 1–17.
9. BLONDEAUX, P. (2001). "Mechanics of Coastal Forms". *Annu. Rev. Fluid Mech.* 33, 339–370.
10. COWEN, E.A. and MONISMITH, S.G. (1997). "A Hybrid Digital Particle Tracking Velocimetry Technique". *Exp. Fluids* 22, 199–211.
11. DEEN, N.G., WESTERWEEL, J. and DELNOIJ, E. (2002). "Two-phase PIV of Bubbly Flows: Status and Trends". *Chem. Engng. Technol.* 25(1), 97–101.
12. DU TOIT, C. and SLEATH, J. (1981). "Velocity Measurements Close to Rippled Beds in Oscillatory Flow". *J. Fluid Mech.* 112, 71–96.
13. EARNSHAW, H.C. and GREATED, C.A. (1998). "Dynamics of Ripple Bed Vortices". *Exp. Fluids* 25(3), 265–275.
14. EARNSHAW, H.C., BRUCE, T., GREATED, C.A. and EASSON, W.J. (1994). "PIV Measurements of Oscillatory Flow over a Rippled Bed". In: 24th *International Coastal Engineering Conference*, Kobe, Japan, pp. 1975–1982.
15. FREDSØE, J. and DEIGAARD, R. (1992). *Mechanics of Coastal Sediment Transport*. World Scientific Publishing Co., Singapore.
16. GARCÍA, M.H., MUSALEM, R. and ADMIRAAL, D.M. (2002). "Exploratory Study of Oscillatory Flow over a Movable Sediment Bed with Particle Image Velocimetry (PIV)". *Proc. Hydraulic Measurements and Experimental Methods Conference*. ASCE(EWRI)—IAHR, Estes Park, CO.
17. HANSEN, E., FREDSØE, J. and DEIGAARD, R. (1994). "Distribution of Suspended Sediment over Wave-generated Ripples". *J. Waterway Port Coastal Ocean Engng.* 120(1), 37–55.
18. HASSAN, Y., PHILIP, O. and SCHMIDL, W. (1993). "Bubble Collapse Velocity Measurements using a Particle Image Velocimetry Technique with Fluorescent Tracers". *ASME-FED* 172, 85–92.
19. HORIKAWA, K. and IKEDA, S. (1990). "Characteristics of Oscillatory Flow over Ripple Models". In: *22nd International Coastal Engineering Conference*, Kobe, Japan. pp. 661–674.
20. JONSSON, I.G. (1966). "Wave Boundary Layers and Friction Factors". *Proceedings of the 10th International Conference on Coastal Engineering*, Tokyo, pp. 127–148.

21. JONSSON, I.G. and CARLSEN, N.A. (1976). “Experimental and Theoretical Investigations in an Oscillatory Turbulent Boundary Layer”. *J. Hydraul. Res.* 14(1), 45–60.
22. KIGER, K.P. and PAN, C. (2000). “PIV Technique for the Simultaneous Measurement of Dilute Two-phase Flows”. *J. Fluids Engng.* 122, 811–818.
23. KLINE, S.J. and MCCLINTOCK, F.A. (1953). “Describing Uncertainties in Single-sample Experiments”. *Mech. Engng.* 75, 3–8.
24. LIU, P.L.-F., AL-BANAA, K.A. and COWEN, E.A. (2004). “Water Wave Boundary Layer Flows above a Rippled Bed”. In: GRUE, J., LIU, P. and PEDERSEN, G. (eds), *PIV and Water Waves, Advances in Coastal Engineering*, World Scientific Publishing Co., Singapore, pp. 1–49.
25. LONGUET-HIGGINS, M.S. (1981). “Oscillating Flow over Steep Sand Ripples”. *J. Fluid Mech.* 107, 1–35.
26. MEI, R. (1996). “Velocity Fidelity of Flow Tracer Particles”. *Exp. Fluids* 22(1), 1–13.
27. MOFFAT, R.J. (1988). “Describing the Uncertainties in Experimental Results”. *Exp. Thermal Fluid Sci.* 1, 3–17.
28. NAKATO, T., LOCHER, F.A., GLOVER, J.R. and KENNEDY, J.F. (1977). “Wave Entrainment of Sediment from Rippled Beds”. *J. Waterway Port Coastal Ocean Div.* 103, 83–99.
29. NIELSEN, P. (1981). “Dynamics and Geometry of Wave-generated Ripples”. *J. Geophys. Res.* 86(C7), 6467–6472.
30. NIELSEN, P. (1992). *Coastal Bottom Boundary Layers and Sediment Transport*. World Scientific Publishing Co., Singapore.
31. NIMMO SMITH, W.A.M., ATSAVAPRANEE, P., KATZ, J. and OSBORN, T.R. (2002). “PIV Measurements in the Bottom Boundary Layer of the Coastal Ocean”. *Exp. Fluids* 33, 962–971.
32. PERRIER, G., HANSEN, E.A., VILLARET, C., DEIGAARD, R. and FREDSØE, J. (1994). “Sediment Transport over Ripples in Waves and Current”. In: *24th International Coastal Engineering Conference* pp. 2043–2057.
33. PRASAD, A.K., ADRIAN, R.J., LANDRETH, C.C. and OFFUTT, P.W. (1992). “Effect of Resolution on the Speed and Accuracy of Particle Image Velocimetry Interrogation”. *Exp. Fluids* 13, 105–116.
34. SATO, S. (1987). “Oscillatory Boundary Layer Flow and Sand Movement Over Ripples”. PhD Thesis, Department of Civil Engineering, University of Tokyo, Tokyo, Japan.
35. SLEATH, J. (1984). *Sea Bed Mechanics*. John Wiley and Sons, New York.
36. SLEATH, J. (1987). “Turbulent Oscillatory Flow over Rough Beds”. *J. Fluid Mech.* 182, 369–409.
37. SMITH, D. and SLEATH, J. (2005). “Transient Ripples in Oscillatory Flow”. *Continental Shelf Res.* 25, 485–501.
38. TRAYKOVSKI, P., HAY, A., IRISH, J. and LYNCH, J. (1999). “Geometry, Migration, and Evolution of Wave Orbital Ripples at LEO-15”. *J. Geophys. Res.* 104(C1), 1505–1524.
39. VILLARD, P. and OSBORNE, P. (2002). “Visualization of Wave-induced Suspension Patterns over Two-dimensional Bedforms”. *Sedimentology* 49, 363–378.
40. VITTORI, G. and BLONDEAUX, P. (1990). “Sand Ripples Under Sea Waves. Part 2. Finite-amplitude Development”. *J. Fluid Mech.* 218, 19–39.
41. VOROPAYEV, S.I., MCEACHERN, G.B., BOYER, D.L. and FERNANDO, H.J.S. (1999). “Dynamics of Sand Ripples and Burial/Scouring of Cobbles in Oscillatory Flow”. *Appl. Ocean Res.* 21, 249–261.
42. WESTERWEEL, J. (1993). “Digital Particle Image Velocimetry”. PhD Thesis, Delft University of Technology, Delft, The Netherlands.
43. WILLERT, C.E. and GHARIB, M. (1991). “Digital Particle Image Velocimetry”. *Exp. Fluids* 10, 181–193.